Dehydration-induced damage and deformation in gypsum and implications for subduction zone processes

N. Brantut,[1,2] A. Schubnel,[1] E. C. David,[3] E. Héripré,[4] Y. Guéguen,[1] and A. Dimanov[4]

[1] Experimental heating tests were performed on Volterra gypsum to study the micromechanical consequences of the dehydration reaction. The experimental conditions were drained at 5 MPa fluid pressure and confining pressures ranging from 15 to 55 MPa. One test was performed with a constantly applied differential stress of 30 MPa. The reaction is marked by (1) a porosity increase and homogeneous compaction, (2) a swarm of acoustic emissions, (3) a large decrease in P and S wave velocities, and (4) a decrease in V_P/V_S ratio. Wave velocity data are interpreted in terms of crack density and pore aspect ratio, which, modeling pores as spheroids, is estimated at around 0.05 (crack-like spheroid). Complementary tests performed in an environmental scanning electron microscope indicate that cracks first form inside the gypsum grains and are oriented preferentially along the crystal structure of gypsum. Most of the visible porosity appears at later stages when grains shrink and grain boundaries open. Extrapolation of our data to serpentinites in subduction zones suggest that the signature of dehydrating rocks in seismic tomography could be a low apparent Poisson's ratio, although this interpretation may be masked by anisotropy development due to preexisting crystal preferred orientation and/or deformation-induced cracking. The large compaction and the absence of strain localization in the deformation test suggests that dehydrating rocks maybe seen as soft inclusions and could thus induce ruptures in the surrounding, nonreacting rocks.

1. Introduction

[2] In subduction zones, rocks from the subducted oceanic crust undergo a series of metamorphic reactions, including dehydration reactions of hydrous minerals such as clays and serpentines. On the basis of rock physics evidence [e.g., *Raleigh and Paterson*, 1965; *Green and Houston*, 1995; *Dobson et al.*, 2002; *Jung et al.*, 2004; *Milsch and Scholz*, 2005; *Jung et al.*, 2009; *Burlini et al.*, 2009] and seismological data [e.g., *Hacker et al.*, 2003; *Yamasaki and Seno*, 2003], metamorphic dehydration reactions have been suggested as a possible origin for intermediate depth earthquakes in subducting slabs. The dehydration embrittlement process may arise from various mechanisms. First, there is a fluid volume change as well as a solid volume change as dehydration reactions proceed. All dehydration reactions

induce a negative solid volume change since the dehydration products are denser than the starting minerals. Thus, porosity is created, and solid compaction can occur [*Rutter and Brodie*, 1988, 1995; *Rutter et al.*, 2009]. If the volume of fluid released is larger than the newly created pore space and if fluid diffusion is precluded (in limited drainage conditions), the fluid pressure increases and the effective confining pressure decreases. This decrease in effective confining pressure can induce ruptures as the material comes back to the brittle field [*Raleigh and Paterson*, 1965; *Heard and Rubey*, 1966; *Murrell and Ismail*, 1976; *Ko et al.*, 1995; *Olgaard et al.*, 1995; *Ko et al.*, 1997; *Wong et al.*, 1997; *Milsch and Scholz*, 2005]. Secondly, the reaction transforms a given set of minerals into a different mineral assemblage, which has intrinsically different properties than the starting material: Its macroscopic strength can be lower [*Rutter and Brodie*, 1988; *Arkwright et al.*, 2008], and the elastic stiffness of individual grains also evolves. The combination of porosity creation and change in elastic properties of the mineral skeleton has also a major influence on the effective elastic stiffness and P and S wave velocities of the rock during dehydration. In particular, *Popp and Kern* [1993] observed dramatic decreases in V_P, V_S and Poisson's ratio during experimental dehydration of lizardite and gypsum.

[3] Two challenging problems encountered in addressing the possible importance of dehydration embrittlement in

[1]Laboratoire de Géologie, École Normale Supérieure, CNRS UMR 8538, Paris, France.

[2]Rock and Ice Physics Laboratory, Department of Earth Sciences, University College London, London, UK.

[3]Department of Earth Science and Engineering, Imperial College London, London, UK.

[4]Laboratoire de Mécanique des Solides, CNRS UMR 7649, École Polytechnique, Palaiseau, France.

subduction are (1) the identification of dehydrating rocks within the subducting slab, for instance using seismic tomography, and (2) the understanding of the controlling factors promoting a macroscopic "embrittlement." In particular, it is still unclear if dehydration reaction can induce strain localization and shear instabilities during deformation [*Hirose et al.*, 2006; *Chernak and Hirth*, 2010; *Gasc et al.*, 2011].

[4] Because of the intrinsic couplings between compaction, fluid release, drainage conditions and mineral properties evolution, and the technical difficulties linked to high-temperature laboratory tests, experimental investigations of the effect of dehydrations on rock deformation still lack from micromechanical understanding. One way to overcome part of the technical difficulties when dealing with high-pressure and high-temperature tests is to study gypsum as an analogue of serpentine-rich rocks at depth [*Ko et al.*, 1997; *Milsch and Scholz*, 2005]. Gypsum undergoes brittle-ductile transition at moderate pressure (around 10 to 20 MPa confining pressure [*Brantut et al.*, 2011]) and dehydration at less than 150°C, which is easily attainable is a triaxial apparatus using oil as a confining medium [e.g., *Ko et al.*, 1997].

[5] In this paper we present a series of dehydration tests performed on Volterra gypsum in a triaxial apparatus, at various confining pressures and differential stresses. The tests presented here consisted in a regular increase in temperature from room temperature to 150°C, at constant confining and differential stress. No deformation was prescribed in addition to that induced by the dehydration reaction under the imposed stress state. P and S wave velocities were monitored and acoustic emissions (AE) were recorded throughout the tests in order to have access to the dynamics of micromechanical and chemical processes. Pore volumometry was used to monitor the extent of reaction during heating (using the method described by *Llana-Fúnez et al.* [2007] and *Rutter et al.* [2009]). The triaxial tests were complemented by in situ observations of gypsum dehydration in an environmental scanning electron microscope (ESEM). The micromechanical processes occurring during dehydration are discussed, and an effective medium model is used to predict the possible seismic signature of dehydrating rocks in nature.

2. Starting Material and Experimental Setup

2.1. Sample Preparation

[6] The material used in our experiments is natural gypsum alabaster from Volterra (Italy). The initial microstructure consists in a relatively fine grained (from 10 to 200 μm) polycrystal. The initial porosity is of the order of 0.5% [*Brantut et al.*, 2011]. Samples of 85 mm in length and 40 mm in diameter were cored in the same block in the same direction. Initial P wave velocity of the whole block was measured at room pressure and temperature, and is around 5250 m s^{-1}, varying from 5000 to 5300 m s^{-1} depending on the location and on the direction of measurement; anisotropy is thus generally less than ∼5%. After coring, the samples were rectified to obtain perfectly parallel ends (with a precision of $\pm 10 \mu$m).

[7] The samples were jacketed in a perforated viton sleeve, and 16 piezoelectric transducers (PZTs) were directly glued onto the samples surface (see Figure 1). Each PZT is made of a piezoelectric crystal (PI ceramic P1255) sensitive either to P waves (normal to the interface, cylinders of 5 mm in diameter, 2 mm in thickness) or to S waves (along the interface, platelets of $5 \times 5 \times 1$ mm), encapsulated in an aluminum holder. The principal resonant frequency of these sensors is around 1 MHz. The electric connection of the signal is ensured by a mechanical contact between a stainless steel piston and the core of a coaxial plug. In the case of S wave sensors, the crystal is glued with Ag-conductive epoxy to ensure a good mechanical coupling with the aluminum holder. One pair of horizontal S wave PZT was glued, in addition to the set of 14 P wave sensitive PZTs. Once the sensors glued, two layers of soft glue were added around the PZTs onto the jacket to ensure sealing. Then, the sample was placed inside the pressure vessel.

2.2. Triaxial Apparatus

[8] The deformation apparatus used for our experiments is an externally heated triaxial oil medium cell [cf. *Brantut et al.*, 2011; *Ougier-Simonin et al.*, 2011]. The confining pressure P_c is directly applied by a volumetric servo pump, and measured by a pressure transducer with an accuracy of 10^{-3} MPa. The axial stress σ_{ax} is controlled by an independent axial piston, actuated by a similar volumetric servo pump. The axial stress is calculated from a pressure measurement at the inlet of the piston chamber and the surface ratio of the piston's ends. A compressive shear stress is systematically ensured by applying an axial stress slightly higher than the confining pressure. In all tests, the minimum differential stress $\sigma_{ax} - P_c$ was of the order of 0.5 MPa.

[9] All the triaxial tests were performed at controlled stress, which is achieved by adjusting the flow from the servo pumps connected to the axial piston and pressure vessel. The axial deformation is measured externally using the average of three eddy current gap sensors fixed to the bottom end of the cell, with a precision of 0.3 μm. Deformation measurements were corrected from the thermal expansion of the loading column, calibrated in the 25–70°C range at the beginning of the heating tests (while dehydration has not yet started) in hydrostatic pressure conditions.

[10] The heating system is external and consists in a silicone sleeve equipped with a heating wire, wrapped around the pressure vessel. Because of the large volume of the cell, the maximum heating rate is 0.3°C min^{-1} only, the advantage of this being that the temperature field is homogeneous in the sample. The temperature is recorded with two thermocouples, one plunged in the confining oil, and one touching the bottom end of the lower steel plug.

### 2.3. Pore Pressure and Pore Volumometry

[11] The initially dry samples were saturated overnight within the pressure vessel using a pair of QUIZIX volumetric servo pumps, at an imposed constant pore pressure $P_f = 5$ MPa. In all the tests, the pore pressure remained constant (to a 10^{-3} MPa precision) throughout the tests by servo-controlled adjustment of the pumps' volume (drained conditions). Both pumps were interconnected and their volume was continuously monitored and recorded (down to 1 μL precision) during heating.

[12] The pore volume change was used to track the extent of reaction, employing a method similar to that of
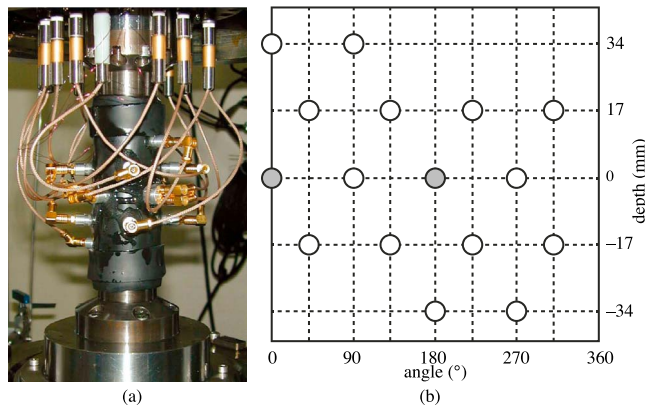
Figure 1. (a) Photograph of the sample assembly and (b) sensor map. The white circles correspond to P wave transducers, and the gray circles are S_h wave transducers.

Llana-Fúnez et al. [2007]. Gypsum dehydrates at around 100°C to produce bassanite [*McConnell et al.*, 1987]:

$$CaSO_4 \cdot 2H_2O \rightarrow CaSO_4 \cdot \frac{1}{2}H_2O + \frac{3}{2}H_2O. \quad (1)$$
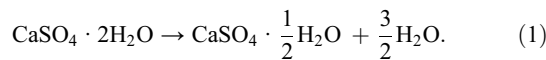
At standard thermodynamic conditions, the molar volume of gypsum, bassanite, and water are 74.7, 53.8, and 18 cm³/mol, respectively [*Robie et al.*, 1979]. Considering the stoichiometry of reaction (1), the total volume change expected at the end of the reaction is $\Delta V_{total} = +8.2\%$, and the solid volume change is $\Delta V_{solid} = -28.0\%$. At the conditions of experiments, i.e., $P_f = 5$ MPa and a temperature T up to 150°C, the total volume change is positive and we expect a net increase in fluid volume during the reaction.

2.4. Experimental Conditions

[13] Three tests were performed in the triaxial rig, under drained conditions, at a constant pore pressure of $P_f = 5$ MPa. Two tests were performed under hydrostatic pressure at $\sigma_{ax} \approx P_c = 15$ MPa and $\sigma_{ax} \approx P_c = 55$ MPa, i.e., 10 and 50 MPa effective confining pressure, respectively. One test was performed under triaxial stress conditions at $P_c = 45$ MPa and $\sigma_{ax} = 75$ MPa, i.e., a total mean stress of 55 MPa and a differential stress of 30 MPa, well below the yield stress of gypsum [*Brantut et al.*, 2011]. Table 1 summarizes the experimental conditions for each test.

[14] All the tests were performed by first increasing the axial, confining and pore pressures up to their target values. Then, the furnace was turned on and the temperature increased steadily at 0.3°C/min, while recording pore volume, deformation, wave velocities and triggered AEs. Because of limited data storage capacity, the continuous AE recording system was only turned on at around 118°C.

2.5. Acoustic Emissions and Elastic Wave Velocities Monitoring

[15] The electric connection from the sensors inside the vessel to the outside is achieved by 16 high voltage coaxial feedthroughs that ensure a high signal-to-noise ratio. The coaxial wires are plugged into high-frequency 60 dB pre-amplifiers with two distinct outputs. One output is continuously recorded at a 4 MHz sampling rate by the Mini

Richter System (ASC Ltd.), and the data are written on the fly onto four separate hard drives (recording 4 channels each). The second output leads to a trigger logic connected to digital oscilloscopes. If the signals verify a given pattern (e.g., a threshold amplitude on a given number on channels in a given time window), they are recorded on the oscilloscopes at a 50 MHz sampling rate. We will thus speak in terms of "streamed data" in the case of continuously recorded signals and "triggered data" in the other case.

[16] In addition to passive AE recordings, active elastic wave velocity surveys were performed. At 5 min intervals during the experiments, a 60 V high-frequency (1 μs rise-time) pulse was sent on each channel while the other channels were recording. This resulted in the emission of a P or S wave (depending on the pulsing sensor), and since the origin time of the pulse and the sensors positions were known, the measurement of the travel times allowed us to calculate the average velocity along each raypath. P wave arrival times were automatically picked using the software Insite (from ASC Ltd.). A reference survey performed at room temperature under hydrostatic pressure was chosen. This "master" survey was processed using the known positions of sensors and picked arrival times to yield an absolute value of the wave velocities. All the waveforms were then cut around the picking time in a 5 μs window and cross-correlated with the master survey, and the position of the maximum of the cross-correlation coefficient indicated the shift in P wave arrival time. This method provides an automatic measurement of the relative P waves velocities evolution during the tests. It cancels the intrinsic errors of manual or automatic picking processes. However, the absolute value may be slightly shifted because of these types of errors in the picking of the master survey. On the other hand, S waves were manually picked and processed independently to calculate individual velocities across the pair of S transducers.

### 2.6. In Situ Imaging Under ESEM

[17] Additional experiments were performed in a FEI QUANTA600 field emission ESEM equipped with a heating stage to observe in situ microstructural changes during the dehydration reaction of gypsum. Small Volterra gypsum disks of 4 mm in diameter and 2 mm in thickness were prepared and polished with 1 μm diamond paste. No conductive coating of the surface was used. The samples were placed on a 1000°C heating stage, cooled by circulating water, built in the vacuum chamber of an environmental scanning electron microscope at the Laboratory of Solid

Table 1. Experimental Conditions for Gypsum Dehydration Tests[a]

Test	P_c (MPa)	P_f (MPa)	T_{max} (°C)	σ_{ax} (MPa)	ϵ_{axial}^{final} (%)	ΔV_Q^{final} (mL)	t_{max} (s)
Vol23	15	5	150	15	1.13	12.8	30580
Vol25	55	5	150	55	4.32	22.3	31420
Vol26	45	5	135	75	9.03[b]	21.7[b]	25710[b]

[a]T_{max} is the maximum temperature experienced by the sample, ϵ_{axial}^{final} is the final axial compaction, ΔV_Q^{final} is the final fluid volume increase measured by the pore pressure pumps, and t_{max} is the duration of the heating test from room temperature up to T_{max}.
[b]Final values reported when the piston reached its maximum motion range (see text and Figure 4).
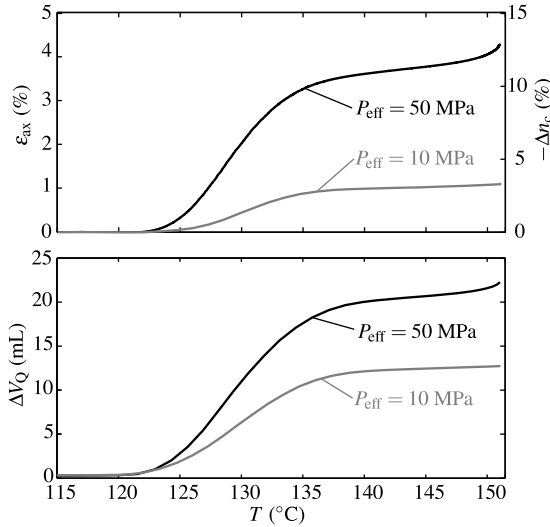
Figure 2. Shortening, compaction, and fluid release during drained hydrostatic heating tests.

Mechanics in École Polytechnique (France). The observations were performed with a high-temperature gaseous secondary electron detector under an accelerating voltage of 20 keV. Water vapor at a pressure of 360Pa was used as the imaging gas. The heating rate was set at 25°C/min up to 80°C and then 10°C/min up to 200°C. On the basis of an approximate heat diffusivity of gypsum of the order of 1 mm^2 s^{-1}, we get a characteristic heat diffusion time of the order of 4 s across the sample. As a 10°C/min heating rate corresponds to a maximum of 0.2°C change per second, the temperature gradient was largely negligible during the heating tests. Pictures were taken every 12 s (i.e., every 2°C).

[18] After these tests, the sample's surface was coated with carbon and observed in high vacuum in a field emission gun SEM at much higher resolution (magnification up to ×50000).

3. Results

3.1. Compaction and Fluid Release

[19] Figure 2 shows the porosity change and the fluid volume change measured by the pore pressure pump during the two hydrostatic tests performed at effective pressures $P_{\mathrm{eff}} = 10$ MPa and $P_{\mathrm{eff}} = 50$ MPa, as a function of temperature. At around 118°C, the fluid volume extracted by the pump increased dramatically, and the sample started shortening. In the hydrostatic tests, axial shortening data is used to estimate volumetric compaction. We assume the deformation is isotropic, which implies that

$$\epsilon_{kk} = 3\epsilon_{\mathrm{ax}}, \qquad (2)$$

where ϵ_{kk} is the volumetric strain and ϵ_{ax} is the axial strain. This approximation is an upper bound for ϵ_{kk} since a nonzero differential stress, of the order of 0.5 MPa, is imposed. At $P_{\mathrm{eff}} = 50$ MPa, the volumetric compaction is 12.9% and the volume of fluid extracted is 22.3 mL, i.e., 20.9% of the sample's initial volume. At $P_{\mathrm{eff}} = 10$ MPa, the volumetric compaction is only 3.2% and the volume of fluid extracted is 12.8 mL, i.e., 12.0% of the sample's initial volume.

[20] Further assuming that all the volumetric strain arises from inelastic compaction of the porosity created during the reaction, we have

$$\Delta n_{\mathrm{c}} = -\epsilon_{kk}, \qquad (3)$$

where Δn_{c} is the porosity change. The measurements of fluid volume release ΔV_{Q} combined with the estimate of porosity change Δn_{c} in the two hydrostatic tests are used to estimate the extent of reaction ξ (see Appendix A):

$$\Delta\xi = \left[\rho_{\mathrm{f}}(T_0) \frac{\Delta V_{\mathrm{Q}}}{V_{\mathrm{sample}}} + \rho_{\mathrm{f}}(T)\Delta n_{\mathrm{c}} \right]$$
$$\left/ \left[\frac{3}{2} \frac{M_{\mathrm{water}}}{M_{\mathrm{gypsum}}} \rho_{\mathrm{gypsum}} - \rho_{\mathrm{f}}(T)\left(1 - \frac{V_{\mathrm{bass}}}{V_{\mathrm{gypsum}}} \right) \right], \right. \qquad (4)$$

where T is the temperature of the cell, T_0 is the room temperature, ρ_{f} is the density of water, V_{sample} is the initial volume of the sample, M_{water} and M_{gypsum} are the molar masses of water and gypsum, ρ_{gypsum} is the density of gypsum, and V_{bass} and V_{gypsum} are the molar volumes of bassanite and gypsum. The density of water is given as a function of temperature at 5 MPa pressure by the software GE0TAB [*Berman*, 1991]. Other parameter values are reported in Table 2.

[21] Figure 3 presents the reaction progress as a function of temperature and the reaction rate as a function time for the two hydrostatic tests. The final reaction extent at 150°C was around 0.85; this estimate is a lower bound, considering that the porosity compaction Δn_{c} is an upper bound (see equation (2)). This value of reaction extent was confirmed by X-ray diffraction spectra obtained on powdered samples prepared from the dehydrated specimens. Although performed at different effective pressures, both experiments have similar reaction rates. This is not unexpected since both tests were performed at the same fluid pressure, which is the relevant thermodynamic parameter for dehydration reactions [*Connolly*, 1997; *Wang and Wong*, 2003].

[22] Using the calculated reaction extent and the measured compaction, the porosity n can be estimated throughout the hydrostatic tests (see equation (B4)). The evolution of n

Table 2. Parameter Values Entering in the Calculation of Reaction Progress and in the Effective Medium Model

Parameter	Symbol	Value	Units
Sample volume	V_{sample}	106.8×10^{-4}	m^{-3}
Molar mass of water	M_{water}	18	g mol^{-1}
Molar mass of gypsum	M_{gypsum}	172	g mol^{-1}
Density of gypsum[a]	σ_{gypsum}	2305	kg m^{-3}
Density of bassanite[a]	σ_{bass}	2700	kg m^{-3}
Molar volume of bassanite[a]	V_{bass}	53.8	cm3 mol^{-1}
Molar volume of gypsum[a]	V_{gypsum}	74.7	cm3 mol^{-1}
Bulk modulus of gypsum[b]	K^0_{gypsum}	41×10^9	Pa
Shear modulus of gypsum[b]	G^0_{gypsum}	16×10^9	Pa
Bulk modulus of bassanite[c]	K^0_{bass}	70×10^9	Pa
Shear modulus of bassanite[d]	G^0_{bass}	30×10^9	Pa
Bulk modulus of water	K_{f}	2×10^9	Pa

[a]From *Robie et al.* [1979].
[b]From *Stretton* [1996] and *Stretton et al.* [1997].
[c]Interpolated value at 120°C from *Comodi et al.* [2009].
[d]The value of the shear modulus of bassanite cannot be found in the published literature; the value chosen here was determined by trial and error to obtain a reasonable fit of the wave velocity data.
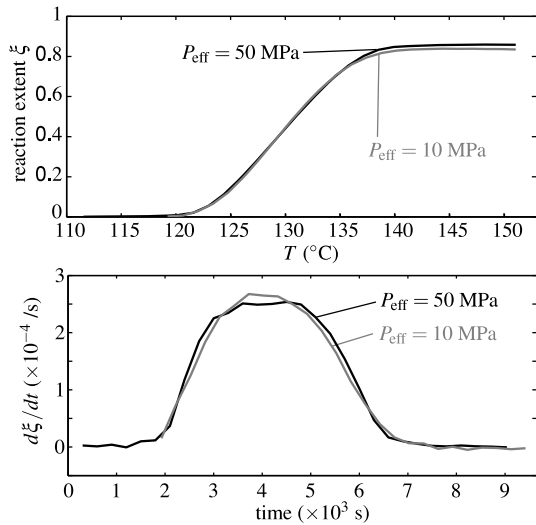
Figure 3. Reaction progress and reaction rate as a function of temperature and time during hydrostatic drained tests. The reaction progress is calculated from porosity compaction and fluid release, using equation (4).

versus ξ is reported later in Figure 12 (top). At $P_{\text{eff}} = 10$ MPa, there is a linear relationship between n and ξ, which implies that the compaction is also a linear function of the reaction extent. At $P_{\text{eff}} = 50$ MPa, the linearity between n and ξ breaks down, which implies that the compaction becomes a nonlinear function of the reaction extent.

[23] Figure 4 shows axial shortening, fluid volume and differential stress data during heating for the test Vol26 performed in creep conditions (constant differential stress). Since this experiment was not performed in an isotropic stress state, equation (2) is not valid and there is no robust way to estimate the reaction progress. During this test, the axial shortening was such that the piston reached its maximum extent of motion before at 135°C. Before this point, the axial shortening reached 9%, and the volume of fluid released was 21.7 mL (i.e., 20.3% of the initial sample
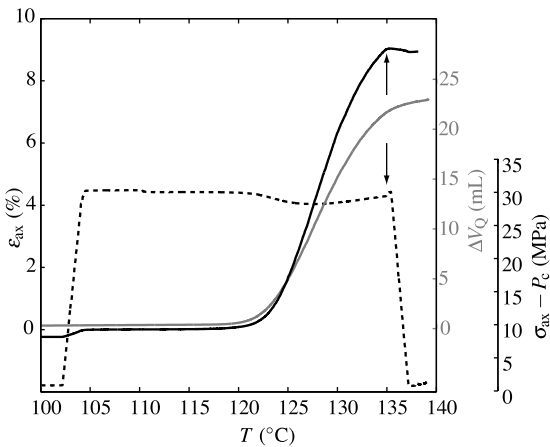

Figure 4. Shortening (solid black line), fluid release (solid gray line) and differential stress (dashed line) during the drained heating test performed in creep conditions at $P_{\text{c}} = 45$ MPa and $\sigma_{\text{ax}} = 75$ MPa. The arrows indicate the piston stroke end.

volume). There was no catastrophic acceleration of the deformation, and the recovered sample did not show any macroscopic faulting. The major difference between this test and the test performed in hydrostatic stress state (Vol25) at the same mean stress is the amount of axial shortening, which is much larger when a differential stress is applied.

3.2. Elastic Wave Velocities

[24] Measurements of P wave velocity (denoted V_{P}) as a function of time for various raypaths are summarized in Figure 5. In order to emphasize the relative changes
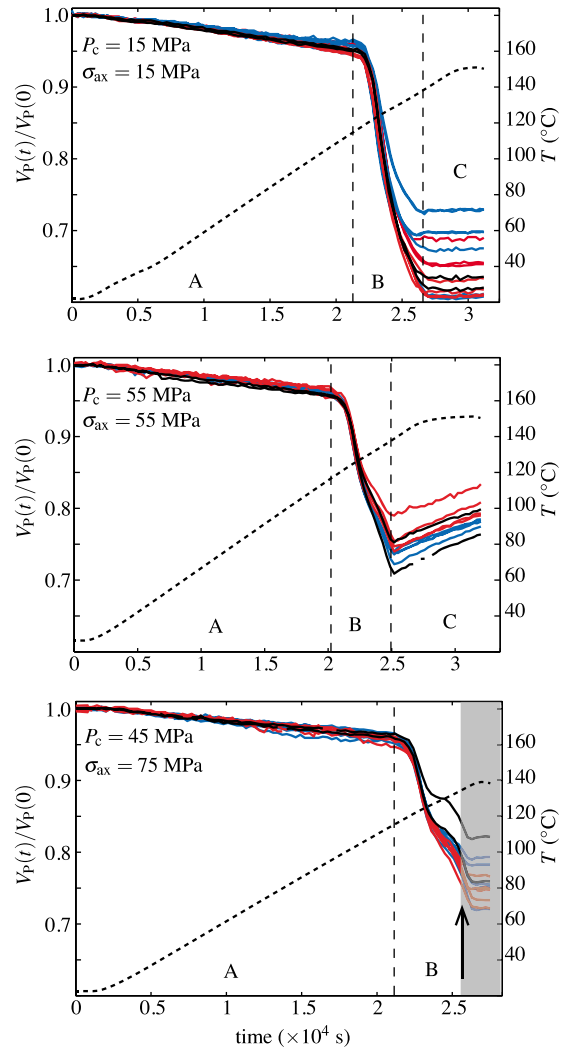
Figure 5. Relative evolution of P wave velocity during dehydration tests. The wave speeds are normalized by their initial value, measured at room temperature and under the stress conditions denoted in the graphs. Temperature is indicated by the dotted line. Black lines denote measurements along raypaths oriented at 30.5° from the vertical. Blue lines correspond to raypaths oriented at 49.6° from the vertical. Red lines correspond to horizontal raypaths. Arrow and gray area in the bottom graph denote the onset of the piston stroke end. Three steps are distinguished. During phase A, V_{p} decreases slowly and homogeneously in the samples. During phase B, dramatic and heterogeneous decreases in V_{p} are recorded. During phase C, P wave velocities slowly increase.
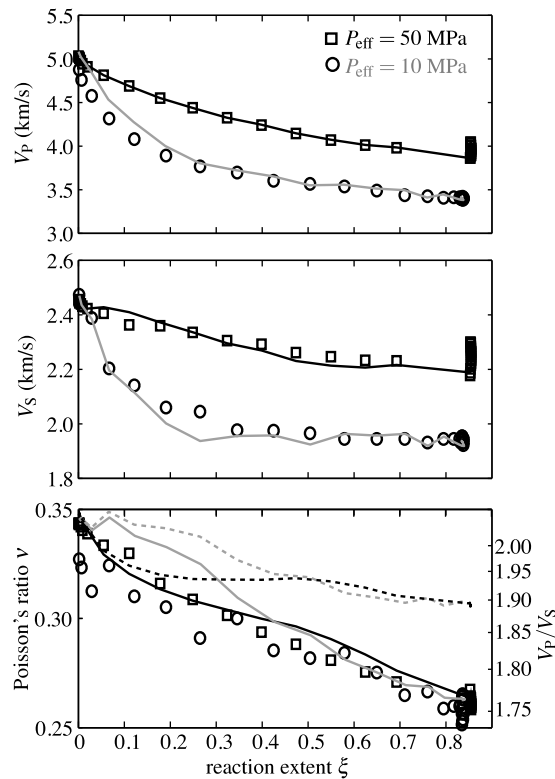
Figure 6. P and S wave speeds and Poisson's ratio during dehydration. Measurements are performed using a single pair of sensors along a horizontal path. Solid black and gray lines correspond to simulations calculated using the effective medium model presented in section 4.1. Dashed lines correspond to a calculated Poisson's ratio that does not account for changes in elastic moduli of the solid skeleton (see section 4.1 for details).

occurring during the dehydration reaction, the ratio of $V_P(t)/V_P(0)$ is plotted, where $V_P(0)$ is the P wave speed along the given raypath measured at room temperature and under the stress conditions of the test. The time series can be divided into three sequences. During sequence A, the temperature increased from room temperature up to 118°C, and the P wave speeds decreased linearly and homogeneously. This decrease in velocity was only moderate, of the order of 5%. Sequence B consists in a dramatic decrease in P wave speeds, from 25% to 40% during the test performed at $P_c = 15$ MPa, and from 20% to 30% during the tests performed at $P_c = 55$ MPa and $P_c = 45$ MPa. Finally, during sequence C the P wave speeds slowly increased. It coincides with post-reaction compaction at temperatures above 140°C. The phase C of the test performed at $\sigma_{ax} = 75$ MPa cannot be interpreted since the end stroke of the piston was reached before the end of the test.

[25] During the hydrostatic tests, the velocities measured along raypaths oriented at the same angle with respect to the vertical (curves of the same color) did not decrease of the same amount. For the test performed at $\sigma_{ax} = 75$ MPa, the data seem to indicate a transversely isotropic velocity field, since horizontal paths generally have slower P wave velocities than low-angle diagonal paths. This will be discussed in section 5.2.

[26] S wave velocity was measured along a horizontal path during the tests. The P wave velocity was also measured between the same pair of sensors, in order to have access to a consistent V_P/V_S ratio. Figure 6 summarizes the measurements of V_P, V_S and V_P/V_S as a function of the extent of reaction ξ for the two hydrostatic tests. During those tests, we assume that the overall material remains isotropic, and the Poisson's ratio is calculated as

$$\nu = \frac{V_P^2 - 2V_S^2}{2V_P^2 - 2V_S^2}. \tag{5}$$

This Poisson's ratio is an effective macroscopic value for the entire core, since our observations indicate that the sample becomes heterogeneous during the dehydration reaction. During the reaction, V_P, V_S, and ν decreased gradually. The decrease in Poisson's ratio did not depend upon the confining pressure at which the reaction occurs.

3.3. Acoustic Emissions

[27] For each experiment, AEs were recorded in trigger mode during the whole test, and the continuous recording was turned on at $T = 118$°C. Three continuous acoustic waveforms, as well as axial shortening and temperature, are displayed in Figure 7.

[28] At $P_c = 15$ MPa, a moderate AE activity started at around 120°C, which also coincides with the onset of axial shortening. AE activity stopped at 135°C. For both experiments performed at 55 MPa mean stress, AEs were significantly more numerous and their amplitude were higher. The AE activity consisted in a swarm that started at 120°C, concomitantly with axial shortening, and became more intense as shortening accelerates.

[29] Figures 8 (bottom) and 9 (bottom) shows the axial shortening rate $\dot{\epsilon}_{ax}$ and the AE rate as a function of time for the two experiments conducted at 55 MPa mean stress. In the hydrostatic case (Figure 8), the AEs swarm coincided with the shortening rate. In the creep test at $\sigma_{ax} = 75$ MPa (Figure 9), the AE swarm started at the onset of the macroscopic axial shortening by but the peak AE activity occurred before the peak shortening rate, and the AE activity died off while the shortening rate kept increasing and reached its peak.

[30] For the two tests performed at 55 MPa mean stress, a significant number of AEs could be located. The localization procedure is a collapsing grid search algorithm described by *Brantut et al.* [2011]. The P wave velocity field used for the location was a stepwise constant homogeneous field, updated every 5 min using the average P wave speed measured in all directions. Because of the strong variations in the P wave velocities measured in the sample, the use of a homogeneous model in the localization algorithm induces a location error of the order 5 mm. For the hydrostatic test performed at $P_c = \sigma_{ax} = 55$ MPa (Figure 8), 1533 individual AEs could be located. Four sequences are distinguished during the AE swarm. Sequence I corresponds to the occurrence of the first 100 AEs, prior to and at the onset of the shortening. Sequence II corresponds to the increase of AE and shortening rates; sequence III spans around the peak AE rate, and sequence IV corresponds to the decrease in AE and shortening rates. The AEs occurring during sequence I are located at the top end of the sample. In the sequences II–IV, they are
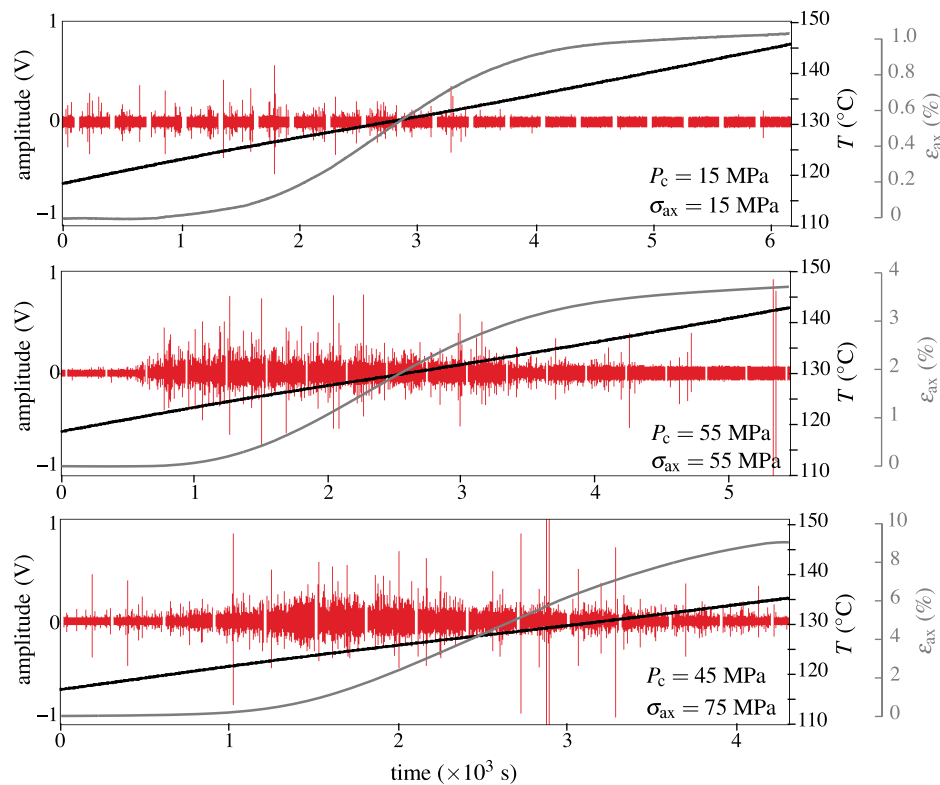
Figure 7. Continuous acoustic waveforms (red), temperature (black line), and axial shortening (gray line) during dehydration tests. White spaces within the waveforms corresponds to active wave velocity surveys. The dehydration reaction, which starts just above 120°C, corresponds to a swarm in acoustic emission (AE) activity.

rather homogeneously distributed, and the AE swarm seems to slowly diffuse within the entire sample. Similarly, for the creep test performed at $P_c = 45$ MPa and $\sigma_{ax} = 75$ MPa (Figure 9), 1374 individual AEs could be located. An additional sequence (0), corresponding to the axial loading of the sample, is distinguished. The AE activity significantly starts during sequence I, in the same fashion as in the hydrostatic case: the first AEs tend to occur at the ends of the sample, and then they are homogeneously distributed.

[31] When good quality AE waveforms were recorded (i.e., if the P wave amplitude is much larger than the background noise), the focal mechanism of the AE could be estimated. First arrival P wave amplitudes were picked, and then inverted by a least squares method to retrieve the source moment tensor of the event. The six components of the moment tensor are projected into the normalized (T, k) space of *Hudson et al.* [1989] (Figure 10), where T (horizontal axis) is a measure of the deviatoric part and k (vertical axis) is a measure of the isotropic part of the moment tensor. In this framework, shear mechanisms lie along the horizontal axis and pure implosions are located in the $k < 0$ part of the plot (within a 30% confidence on k [*Feigner and Young,* 1992]). Figure 10 shows focal mechanisms of 95 events from experiment Vol25 (hydrostatic) and 65 events from experiment Vol26 (creep). The events are chosen evenly throughout each test. In experiment Vol25 (hydrostatic), all the focal mechanisms correspond to mixed shear cracks and implosions, and no AEs are significantly in the tensile side of the graph. The situation is qualitatively similar for

experiment Vol26 (creep), where most AEs correspond to shear, some of them having a significant negative volumetric component. Although our data set of inverted moment tensors is limited, the variety of mechanisms seems to be wider in the creep experiment.

3.4. Microstructure Evolution During Dehydration

[32] Additional tests were performed in low vacuum (360 Pa chamber pressure) under the ESEM, allowing us to visualize in situ the microstructural changes occurring during the dehydration of gypsum.

[33] Figures 11a, 11b, and 11c correspond to a sequence of pictures of a gypsum grain taken at 25°C, 120°C and 143°C, respectively. The grain remained intact during heating from 25°C up to around 120°C, when microcracks started to appear inside the grain. All these cracks were in the same orientation, and seemed to have very low aspect ratio. At 143°C, numerous aligned thin cracks were inside the grain, and the grain boundaries started opening (aperture of the order of 1μm). Opening of grain boundaries created much wider cracks, i.e., with higher aspect ratios than the intragranular aligned thin cracks. Similar observations were performed on two other samples, ensuring a good reproducibility. The resolution of the ESEM and the fact that the observations were made on a free surface prevents us from drawing any strong conclusion as regards the relative timing of the formation of the intragranular versus intergranular cracks. Indeed, *Ko et al.* [1997] observe that nuclei of bassanite first appears at grain boundaries. Nevertheless,
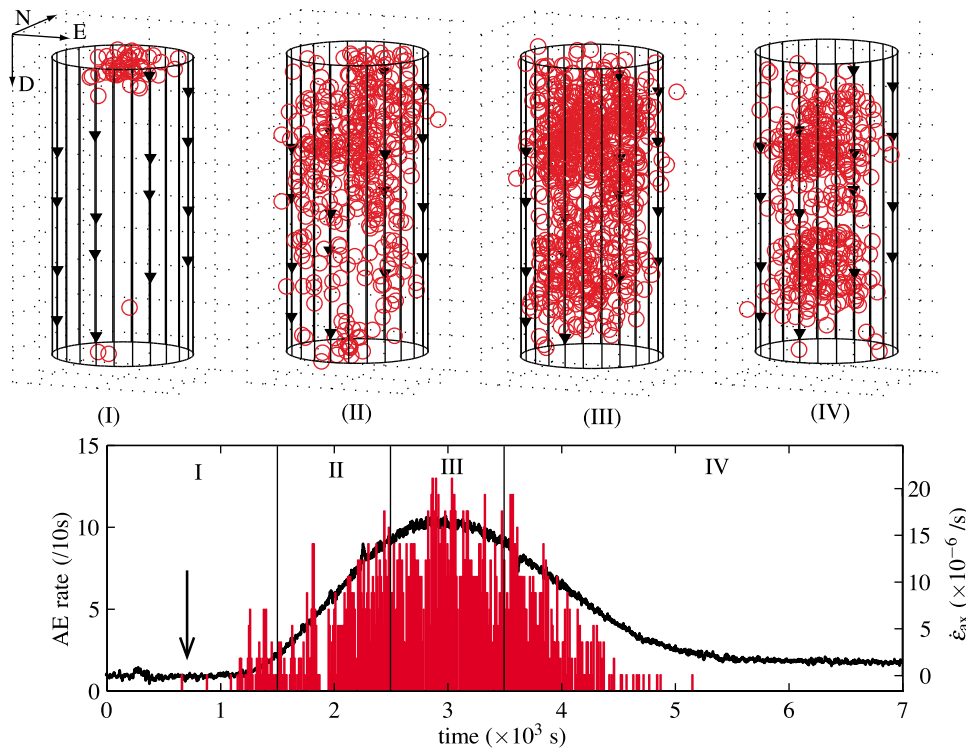
Figure 8. Spatiotemporal distribution of AEs, AE rate, and shortening rate during the test performed at $P_c = \sigma_{ax} = 55$ MPa. AEs occurring during phase I are localized at the top end of the sample, close to the pore fluid outlet. AEs are then more homogeneously distributed throughout the sample (phases II–IV). AE activity stops concomitantly with axial shortening. The arrow indicates the onset of wave velocity decrease.

our observations indicate that two distinct microcrack families can exist, and that they correspond to two different structural levels. The in situ observations carried out in the ESEM were complemented by additional observations in a field emission gun SEM (FE-SEM, Figures 11d, 11e, and 11f). The orientation of the intragranular cracks within a given grain is clearly not random (Figures 11d and 11e). In particular, the microstructure often features band-like structures with evenly spaced, parallel thin cracks (Figure 11f). This can be understood by considering that the orientation of dehydration-induced cracks is dictated by the crystallographic orientation of the starting gypsum grain (as demonstrated by *Sipple et al.* [2001]). In particular, *Sipple et al.* [2001] note that most cracks appear along the (010) planes of gypsum, where water molecules lie. The cracks observed in Figure 11f could indicate the orientation of (010) planes in the host gypsum crystal.

[34] X-ray diffraction measurements performed on powdered samples after observation indicate that the material was pure bassanite.

4. Interpretations and Discussion

4.1. Elastic Wave Velocities Evolution

#### 4.1.1. Thermal Dependency of Elastic Moduli

[35] The linear decrease in P and S wave velocities during heating up to 110°C (before dehydration) can be explained either by thermal cracking, or by the thermal dependency of gypsum's elastic moduli. Thermal cracking is likely to be unimportant here, since the change in velocities occurs at all temperatures at a constant rate, and is of the same order of magnitude (around 5%) for the tests performed under various confining pressures. The finite deformation due to thermal expansion of gypsum is of the order of 10^{-5} °C^{-1} and does not suffice to explain the variation in velocity. By using the relations

$$V_P = \sqrt{\frac{K + (4/3)G}{\rho_s}}, \qquad (6)$$

$$V_S = \sqrt{\frac{G}{\rho_s}}, \qquad (7)$$

where K is the bulk modulus, G is the shear modulus and ρ_s is the density of Volterra gypsum, we calculate the variations of G and K with respect to temperature in the range 25°C–100°C. Only horizontal P and S waves are used. Assuming that the starting porosity is negligible, the density of pure gypsum is used. The results for $\partial G/\partial T$ and $\partial K/\partial T$ are reported in Table 3, where the error on the derivatives corresponds to an error of $\pm$ 100 m/s on the velocity measurements. The value of $\partial G/\partial T$ is of the order of -12 MPa °C^{-1}, and the value of $\partial K/\partial T$ is of the order of -35 MPa °C^{-1}. The orders of magnitude for $\partial G/\partial T$ and $\partial K/\partial T$ are comparable to typical temperature dependencies of common minerals [*Ahrens*, 1995]. It is thus likely that most of the variations in wave velocities observed in
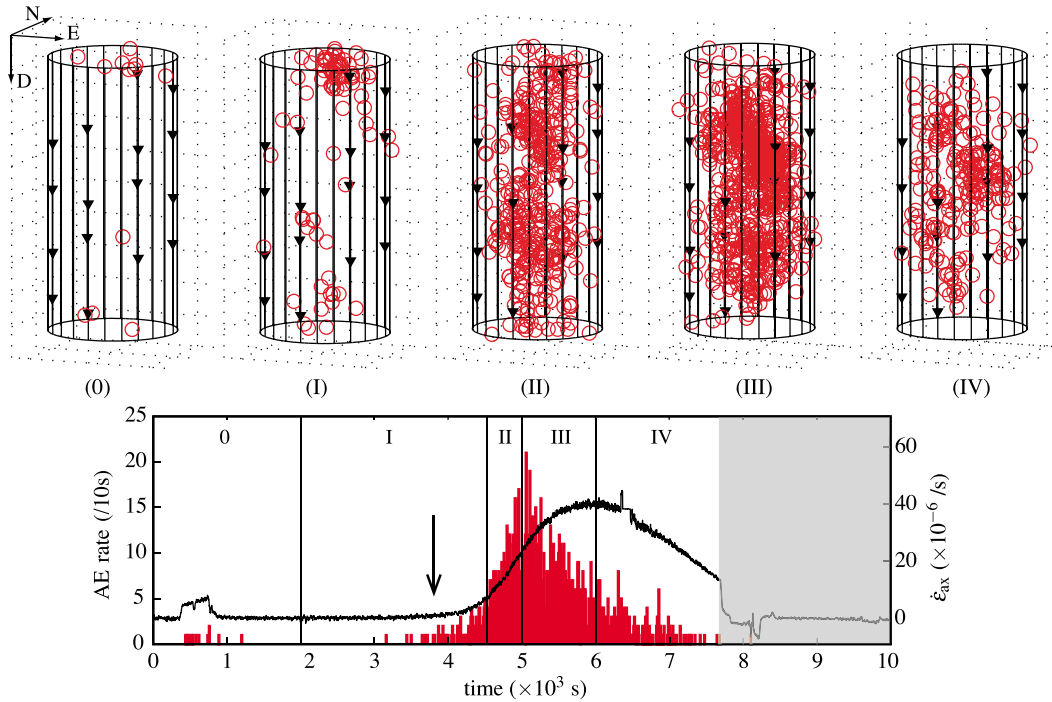
Figure 9. Spatiotemporal distribution of AEs, AE rate, and shortening rate during the test performed at P_c = 55 MPa and σ_{ax} = 75 MPa. Phase 0 corresponds to the axial loading up to the target axial stress; no significant AE activity is recorded during this step. AEs occurring during phase I are localized at the top end of the sample, close to the pore fluid outlet. AEs are then more homogeneously distributed throughout the sample (phases II–IV). AE activity stops concomitantly with axial shortening. The arrow indicates the onset of wave velocity decrease. The shaded area corresponds to the end stroke of the piston.

the 25°C–100°C range are due to the thermal dependency of elastic moduli of gypsum.

4.1.2. Effective Medium Modeling

[36] During the dehydration reaction, as the mineral composition of the rock evolves, a considerable porosity is created. Cracks and pores are known to have a major effect on elastic velocities [*Walsh*, 1965; *Budiansky and O'Connell*, 1976; *Guéguen and Palciauskas*, 1994]. By assuming that pores can be represented by idealized shapes, such as spheroids, it is possible to quantitatively interpret wave velocities in terms of microstructure [*Kuster and Toksoz*, 1974; *Zimmerman*, 1991a; *Sayers and Kachanov*,
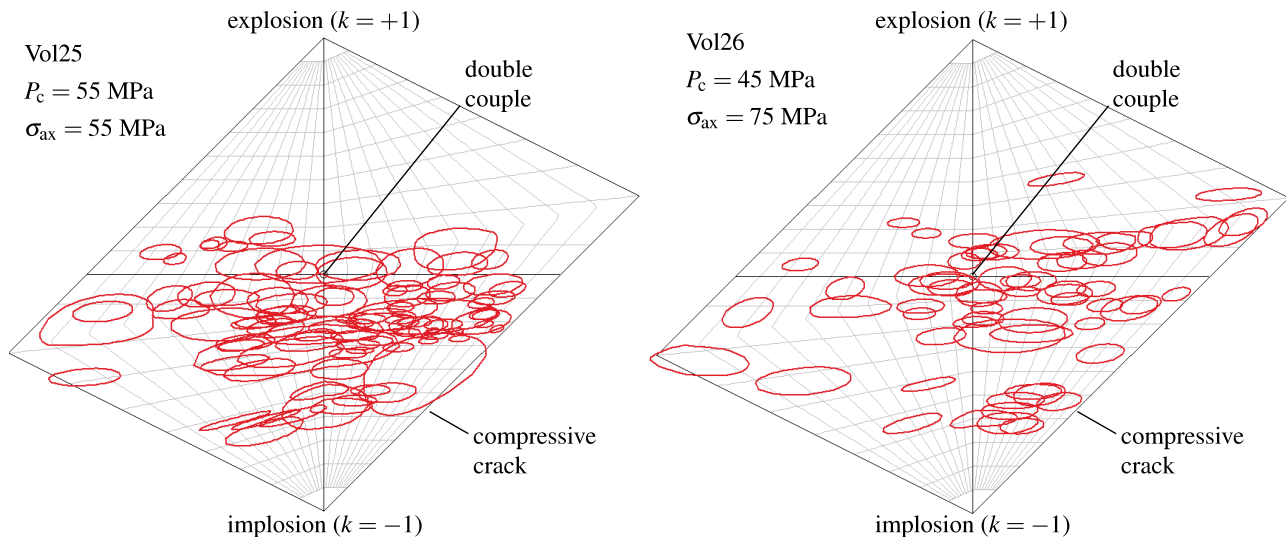
Figure 10. Focal mechanisms for (left) 95 AEs from experiment Vol25 and (right) 65 AEs from experiment Vol26 in a T-k plot [*Hudson et al.*, 1989]. The size of the red ellipsoids corresponds to the uncertainties.
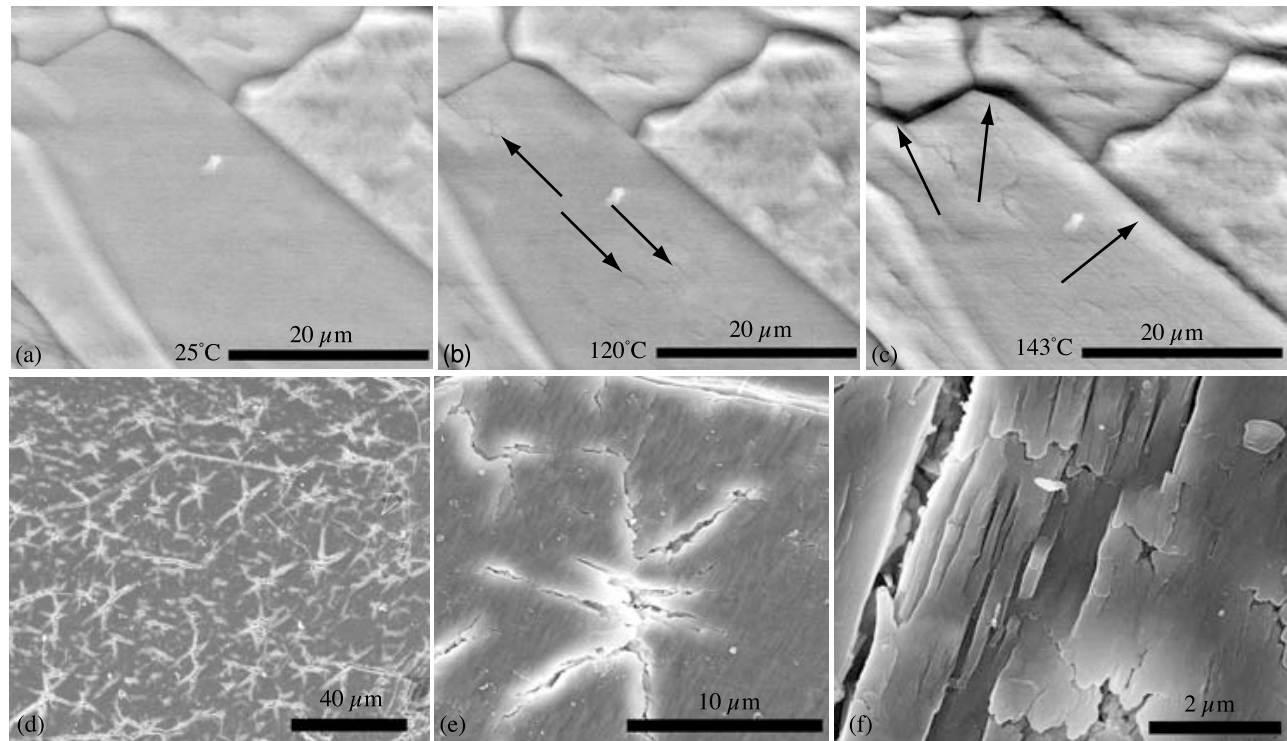
Figure 11. Microstructure evolution (a–c) during and (d–f) after dehydration. Secondary electron mode. Figures 11a–11c were taken in situ, without coating, at 360 Pa chamber pressure. At around 120°C, intragranular cracks appear and grow. Then, grain boundaries progressively open. Figures 11d–11f were taken on the same sample, after carbon coating, in a FE-SEM under an accelerating voltage of 10 kV. Orientations of intragranular cracks are not random and are likely to be dictated by the crystal orientation of initial gypsum grains [*Sipple et al.*, 2001].

1995]. In the two hydrostatic tests, we assume that the overall effective medium remains isotropic and can be represented by a solid matrix containing one family of randomly oriented spheroids, having one average aspect ratio α.

[37] For negligibly small values of α (thin cracks), simple analytical solutions exist that relate the effective elastic moduli to the crack density parameter [*Walsh*, 1965; *Henyey and Pomphrey*, 1982; *Zimmerman*, 1991a; *Sayers and Kachanov*, 1995; *David and Zimmerman*, 2011a]. The crack density parameter γ is related to the porosity by

$$\gamma = \frac{3n}{4\pi\alpha}. \tag{8}$$

The large sample porosities (reaching 20% at the end of the tests) would involve crack densities that are unrealistically high: for $\alpha = 10^{-2}$ and $n = 0.2$, we get $\gamma = 4.8$. Hence, the

use of a thin-crack model is irrelevant for our tests, and we cannot make any a priori assumption on the aspect ratio α.

[38] In addition, it does not seem appropriate to ignore the interactions (of stress and strain fields) between the numerous pores. In other words, the effective moduli cannot be found by simply adding up the individual pore contributions. We use a differential effective medium (DEM) model [*Salganik*, 1973; *McLaughlin*, 1977; *Norris*, 1985; *Zimmerman*, 1991b], in which interactions are taken into account in an approximate way. Pores are successively introduced into the medium in small increments, the new effective moduli being recalculated at each step using the dilute-concentration approximation. This leads to a pair of differential equations giving the effective moduli (K, G) as functions of the porosity n, the elastic moduli of the solid matrix (K^0, G^0), and the mean pore aspect ratio α. Details on the model are reported in Appendix B.

[39] The reaction extent calculated by formula (4), combined with the compaction data, provides an estimate of the porosity n during the reaction (equation (B4); see Figure 12, top). The elastic moduli of the solid matrix are an evolving combination of the elastic properties of gypsum and bassanite. In absence of any information on their spatial arrangement, we assume that the solid matrix moduli are geometric means of gypsum and bassanite moduli (equations (B2) and (B3)). Using the geometric mean ensures that the calculated average of compressibilities is consistent with the average of incompressibilities [*Tarantola*, 2006] (note that

Table 3. Thermal Dependency of Shear Modulus G and Bulk Modulus K of Volterra Gypsum, Measured From Horizontal V_P and V_S

Experiment	$\partial G / \partial T$ (MPa °C^{-1})	$\partial K / \partial T$ (MPa °C^{-1})
Vol23	-12.2 ± 0.6	-41.3 ± 2.0
Vol25	-14.1 ± 0.6	-32.0 ± 1.8
Vol26	-11.8 ± 0.5	-35.0 ± 1.7
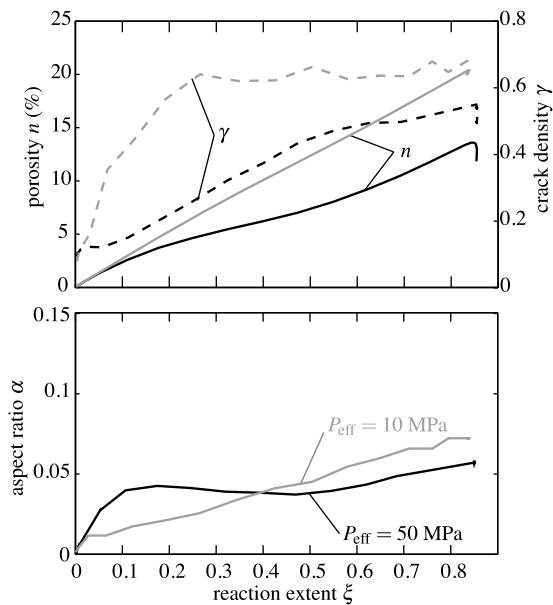
Figure 12. Evolution of (top) porosity and crack density and (bottom) aspect ratio during dehydration in a hydrostatic stress state. Porosity is calculated from equation (B4); crack density is calculated from equation (8). Aspect ratio results from the inversion procedure are detailed in Appendix B.

the result does not differ significantly from that obtained from a Voigt-Reuss-Hill average). Thus, the only unknown parameter is the aspect ratio α of the spheroidal pores. It can be constrained by inverting the effective elastic moduli, which are obtained from P and S wave velocity measurements. For simplicity, we invert for a unique aspect ratio for all the spheroids, which can be viewed as a mean aspect ratio. The inversion procedure is detailed in Appendix B. The parameters used in the inversion are summarized in Table 2.

[40] The inversion results are reported in Figure 12 for the two tests performed in hydrostatic conditions. Figure 6 shows the modeled V_P and V_S and Poisson's ratio. The overall quality of the fits is reasonable, except for the evolution of Poisson's ratio at the onset of the reaction in experiment Vol23 (low effective pressure). This problem may arise from the assumption of zero initial porosity, which is probably wrong at low effective pressure (all the cracks are not closed). However, the misfit vanishes rapidly as dehydration progresses, because the initial porosity becomes negligible compared to the created porosity. At $P_{eff} = 50$ MPa, once the reaction progress ξ reaches 0.1, the aspect ratio reaches $\alpha \approx 0.05$, and remains approximately constant. At $P_{eff} = 10$ MPa, the average aspect ratio increases slowly from around 0.015 to 0.06 throughout the reaction. Such values corresponds to relatively inflated cracks (oblate spheroids). Remarkably, the effective confining pressure, in the range 10–50 MPa, does not seem to affect strongly the shape of the pores created during the dehydration process. This can be explained by considering that the pressure required to close these pores is of the order of $\alpha E \approx 3$ GPa [*Walsh*, 1965] (E being the Young's modulus of the medium).

[41] The crack density γ (calculated from relation (8)) becomes rapidly larger than 0.1 (permeability percolation threshold) during the reaction, and increases up to 0.5

(at $P_{eff} = 50$ MPa) and 0.7 (at $P_{eff} = 10$ MPa). The crack network is thus well within the fully connected percolation regime [*Guéguen and Dienes*, 1989]. At the end of the test performed at $P_{eff} = 50$ MPa, the aspect ratio remains constant and both the crack density and the porosity decrease. Hence, the post reaction compaction induces a change in the size or the number of pores, but does not alter their shape.

[42] The effective medium model explains quantitatively well the observed decrease in Poisson's ratio during the reaction. This decrease can be attributed to (1) the replacement of gypsum (a compliant mineral) by bassanite (a stiffer compound) and (2) the porosity creation. We can establish the respective role of each process by calculating the effective Poisson's ratio expected from the sole contribution of the newly formed porosity (using the inverted aspect ratios), assuming that the solid phases' properties remain constant ((K^0, G^0) fixed). The result is shown in Figure 6 (dashed lines), and indicates that the phase replacement contributes to around 45% of the change in Poisson's ratio.

4.2. AEs Distribution

[43] At the onset of the reaction, AEs are mostly located at one end of the sample, close to the pore fluid outlet; then, they are rather homogeneously distributed throughout the sample. Focal mechanisms are mostly in shear with a large negative volumetric component. We conclude that the AEs are associated with compaction of the porosity created by the solid volume change of the reaction. The distribution of AEs during phase I can be related to fluid diffusion: if the fluid is static, it can sustain, at least partially, the porous structure. This is all the more efficient when the local fluid pressure is elevated (the total volume change of the reaction is positive). Because of the pressure difference between the local dehydrating region and the pore fluid outlet which remains at an imposed $P_f = 5$ MPa, the fluid moves and the porosity is no longer sustained, which results in rapid compaction. As evidenced by the values of crack density > 0.1 determined from the DEM inversions, the porosity creation during the reaction contributes to the formation of a percolation network that allows the drainage of the fluid (see also *Fusseis et al.* [2011]). Only one connected path through the whole sample might be enough to ensure homogeneous drainage conditions and thus to allow homogeneous compaction, in a similar fashion to homogeneous pore collapse observed in high-porosity sandstones [*Fortin et al.*, 2009]. This can explain the rather homogeneous distribution of AEs during phases II–IV.

[44] In Figures 8 (bottom) and 9 (bottom) (black arrows) we note that the onset of wave velocity decrease occurs before the onset of the AE swarm. It implies that damage is induced nondynamically at the initiation of the reaction. This initial stage can be related to the intragranular cracks of a few microns length that appear at the onset of the reaction, observed during the in situ ESEM tests. The pores that compact dynamically and produce AEs could be opened at the grain boundaries at later stages during dehydration, as shown by the ESEM tests.

5. Extrapolations and Implications for Subduction Zones

5.1. Extrapolation to Low-Frequency Seismic Waves

[45] The measurements of V_P, V_S, and V_P/V_S during the dehydration tests were performed with high-frequency

(of the order of 1 MHz) piezoelectric transducers. Similar properties are determined by seismic tomography in the field, but at much lower frequency (around the 1 Hz). Dry materials do not exhibit any frequency dependence of their elastic constants, however this is not the case when pores are saturated with fluid [*O'Connell and Budiansky*, 1974; *Mavko and Nur*, 1975; *Wang and Nur*, 1990; *Adelinet et al.*, 2010]. When a high-frequency wave passes through, each pore behaves as individually undrained: the induced pore pressure differences between the various pores have no time to equilibrate, and the measured effective elastic moduli are "unrelaxed". When the frequency decreases, the fluid has sufficient time to move locally from one pore to another. At low frequencies, the pore pressure remains uniform throughout its entire volume, and the rock behaves as undrained.

[46] In order to extrapolate the wave velocity measurements carried out in the laboratory to seismological data at the field scale, we first calculate the drained (or equivalently, dry) moduli (K_d, G_d) from the DEM model, using the inverted values for the aspect ratios and in absence of fluid ($\zeta = 0$, see Appendix B). Then, following *Le Ravalec and Guéguen* [1996], the elastic moduli expected at low frequency are calculated by the Gassmann equation of poroelasticity, which relates the undrained bulk modulus K_u to the drained bulk modulus K_d, the bulk modulus of the solid matrix K_0, the bulk modulus of the fluid K_f and the porosity n:

$$K_u = K_d + \frac{(1 - K_d/K^0)^2}{n/K_f + (1 - K_d/K^0 - n)/K^0}. \qquad (9)$$

The shear modulus of the undrained, saturated medium is exactly equal to the dry shear modulus G_d.

[47] The results for Poisson's ratio are shown in Figure 13. In the dry (or, equivalently, drained) cases, the Poisson's ratio decreases dramatically down to $\nu \approx 0.13$, which is expected if a significant concentration of pores having an aspect ratio of ∼0.5 is added in an elastic solid [see *David and Zimmerman*, 2011b, Figure 15]. The low-frequency bound for Poisson's ratio evolution during dehydration is higher than the measurement performed at high frequency. However, the decrease remains significant. This estimation ensures that the seismic tomography signature of dehydrating gypsum in nature is expected to be a decrease in effective Poisson's ratio.

[48] The DEM model with evolving solid matrix was applied here to gypsum but it could be used to predict the elastic moduli of any dehydrating rock type, provided that the average crack aspect ratio can be determined (or assumed). It should be noted that the sense of evolution for Poisson's ratio is not obvious. First, the contribution of the porosity creation on ν is highly sensitive to the pore aspect ratio and to the ratio of fluid and solid compressibilities, and can well result in an increase in ν. For instance, *Fortin et al.* [2007] report an increase in V_P/V_S ratio during cataclastic compaction of a porous sandstone, which was attributed to a replacement of equant pores by thin cracks, i.e., a change in mean pore aspect ratio. On the other hand, the contribution of the solid matrix change depends on the Poisson's ratio of the newly formed mineral assembly, which is not necessarily lower than that of the starting material. In the case of serpentinite dehydration, the two contributing processes (the solid phase change and the porosity creation) also lead to a net decrease in Poisson's ratio, as reported experimentally by *Popp and Kern* [1993], at least in upper crustal pressure ranges.

5.2. Heterogeneity and Anisotropy

[49] The P wave velocity measured during the experiments does not decrease by the same amount along all the raypaths (Figure 5). As explained previously, this can be due to local heterogeneities or a non axisymmetric anisotropy development. One explanation is that the dehydration reaction occurs heterogeneously within the rock, as it is influenced by drainage conditions and the temperature field. Another possibility is that the dehydration-induced cracking reveals initial, centimeter scale heterogeneities in the rock. As shown by *Sipple et al.* [2001] and confirmed by our microstructural observations, the cracking induced by the solid volume change of the reaction develops according to the initial crystal orientations. The dehydration reaction thus induces a strong anisotropy in individual grains due to crack preferred orientation. Volterra gypsum in an evaporitic rock, and groups (up to centimeter scale) of neighboring grains with similar crystal orientations are commonly found (see *Fusseis et al.* [2011] for a detailed investigation of the fabric of Volterra gypsum). The onset of dehydration can thus be marked by the development of heterogeneities in elastic properties.

[50] In the creep test, additional axial deformation is induced during dehydration. During axial deformation of brittle solids, it is generally expected to observe a crack-induced anisotropy due to the development of vertical cracks and preferential closure of horizontal cracks [e.g., *Gupta*, 1973; *Lockner and Byerlee*, 1977; *Ayling et al.*, 1995; *Schubnel et al.*, 2003]. In order to distinguish the possible existence of such an anisotropy during the dehydration test performed in creep conditions, the P wave velocity is averaged out for each orientation of propagation. The evolution of the normalized average V_P in the three available orientations (90°, 49.6°, 30.5° from the vertical axis) is given in Figure 14 (solid lines). Using a transversely isotropic formulation for weak anisotropy [*Thomsen*, 1986], we can estimate the P wave velocity along the propagation angle ϕ by

$$V_P(\phi) = \frac{1}{2} V_0 [(1 + a) - (1 - a) \cos(\pi - 2\phi)], \qquad (10)$$

where V_0 is the P wave velocity along the vertical and a an anisotropy index (equal to $1 + \epsilon$ in the notations of *Thomsen* [1986]). The anisotropy index can be inverted from the normalized velocity evolution by a standard least squares method; it is reported in Figure 14. The corresponding fitted P wave velocities are shown by dashed lines in Figure 14 (top). There is an overall agreement between the predicted and observed velocities. The anisotropy index decreases as dehydration progresses: the horizontal axis becomes a slow axis when compared to the vertical axis, which is a typical signature of vertical microcracks formation and/or preferential closure of horizontal cracks. Note that this crack-induced anisotropy is superimposed to the global heterogeneity in P wave speeds. We see here that mineral dehydration, when occurring under moderate differential stress conditions, might favor the development of a "dehydration-induced crack anisotropy" through the combination of deformation-induced
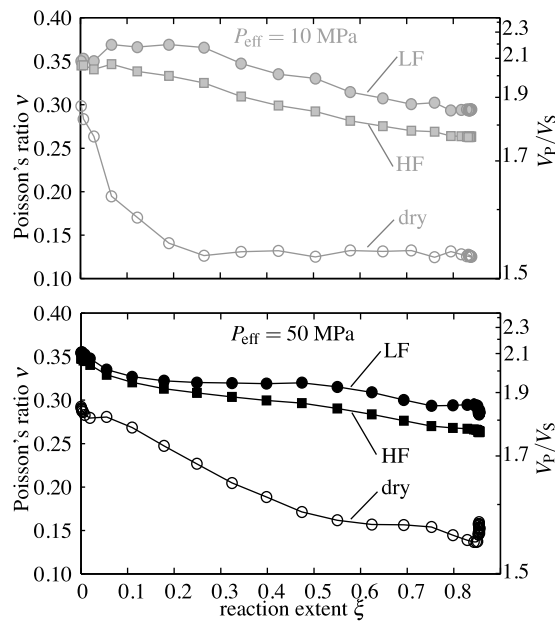
Figure 13. Poisson's ratio evolution during dehydration extrapolated to low-frequency waves using the differential effective medium (DEM) model (see section 4.1.2). HF, high frequency; LF, low-frequency bound, computed using Gassmann theory; dry, dry (or, equivalently, drained) result using the DEM model in absence of fluid.

vertical microcracks, dehydration-induced microcracks of random orientations, and preferential closure of the newly created horizontal cracks.

5.3. Implications for Subduction Zone Processes

[51] As stated in section 1, Volterra gypsum has been chosen as a low-temperature analogue of serpentinites. The extrapolation of our observations on gypsum to serpentine-rich rocks in subduction zones relies on the common structure and properties of both minerals.

[52] Compared to gypsum, serpentine minerals have a similar sheet-like crystal structure with H_2O molecules along cleavage planes [*Deer et al.*, 1966]. The dehydration of serpentine also induces a large negative solid volume change (of the order of 25%). It is thus likely that dehydration of serpentines also induces preferably oriented intragranular cracks along these cleavage planes. Indeed, preliminary in situ ESEM dehydration tests performed on lizardite indicate such features. Wave velocity measurements during serpentinite dehydration performed by *Popp and Kern* [1993] also indicate a decrease in V_P/V_S ratio. The micromechanical model detailed in section 4.1.2 predicts a decrease in the V_P/V_S ratio because of (1) the formation of low aspect ratio porosity and (2) the replacement of soft minerals by stiffer reaction products, as is the case during serpentine dehydration. The extrapolation to low-frequency seismic waves supports the conclusion that the signature of dehydrating rocks in seismic tomography could be a decrease in V_P/V_S. One issue that can be raised is the fact that all our tests were performed in drained conditions. Indeed, the common interpretation is that the V_P/V_S ratio increases with increasing pore pressure [e.g., *Christensen*, 1984; *Peacock et al.*, 2011], which is likely to occur in undrained

conditions during dehydration. Microscopically, pore pressure acts within the pores and induces changes in pore aspect ratios. This effect is likely to be negligible on the overall effective elastic moduli evolution during dehydration since the first-order effects are the creation of microcracks and a change in mineralogy of the rock. In addition, the expected increase in pore pressure during the dehydration reaction in undrained conditions may prevent crack closure even at large depth. The progressive drainage of the fluid could induce progressive crack closure and the wave velocity anomalies could be subsequently reduced.

[53] In subduction zones, serpentine-rich rocks are deformed and may well develop a crystal preferred orientation [*Katayama et al.*, 2009]: in such a situation, the dehydration reaction can induce an additional anisotropy, as well as the expected strong decrease in V_P and V_S. We emphasize here that the definition of Poisson's ratio becomes ambiguous when the material becomes anisotropic; the interpretation of V_P/V_S ratio in seismic tomography is thus not straightforward. To illustrate this point, we show in Figure 14 the apparent Poisson's ratio calculated from (1) the fastest (along a diagonal path) and (2) the slowest (along the horizontal path) P wave speed measured during the test performed with differential stress (in which significant anisotropy is developed). Depending on the orientation of the raypath, the calculated apparent Poisson's ratio can be either stable (if the fastest P wave is used) or significantly decreasing (if the slowest, horizontal P wave is used). As suggested by *Reynard et al.* [2010], anomalous V_P/V_S can sometimes be interpreted as deformation-induced anisotropy without requiring high pore fluid pressure.

[54] The AEs recorded during the dehydration experiments correspond to compaction at the pore scale: they correspond to microscopic processes and cannot be directly interpreted as laboratory analogues of earthquakes. Thus, we do not interpret the AE swarms as dehydration-induced microseismic activity. However, the AE data suggest that compaction is only allowed by drainage of the fluid. In a subducting slab containing serpentinites, drainage conditions would thus influence the spatiotemporal distribution of deformation episodes. Indeed, the interplay of drainage and compaction has already been observed during decarbonation tests of quartz-bearing marbles by *Milsch et al.* [2003].

[55] During the test performed in creep conditions (at constant differential stress), no macroscopic fracture was observed. It is consistent with dehydration tests performed on serpentinite by *Chernak and Hirth* [2010, 2011], which do not bring any evidence of faulting. In perfectly drained conditions, dehydrating rocks do not undergo catastrophic embrittlement (e.g., stick-slip); however, one fundamental characteristic is the important deformation allowed by porosity compaction. Dehydrating rocks in a subducting slab can thus act as temporarily soft inclusions, which would concentrate strain and stress around them. If stress relaxation in the surrounding materials is not fast enough compared to the compaction rate within the dehydrating rocks, the surrounding rocks may experience faulting. Such a rupture mechanism has already been suggested by *Kirby* [1987] for phase transitions with negative solid volume change. The weakness of dehydrating rocks, as confirmed by our mechanical data, suggest that dehydration-induced faulting could be possible even in drained conditions, but only
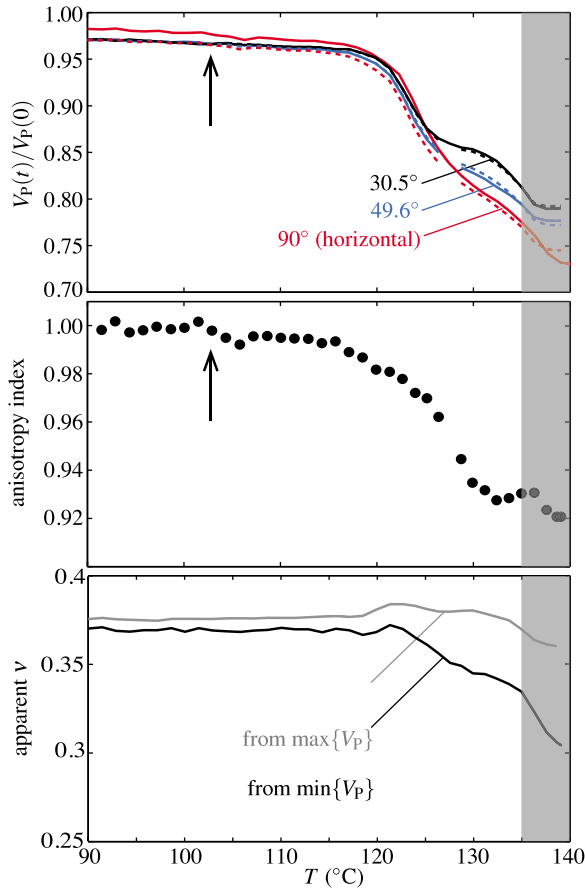
Figure 14. (top) Normalized, average P wave speeds in the three available orientations and (middle) anisotropy index evolution during the test performed at $P_c = 45$ MPa and $\sigma_{ax} = 75$ MPa. (bottom) Two apparent Poisson's ratios calculated from the fastest (gray line) and the slowest (black line) P wave speeds measured during the test. The shaded area corresponds to the stroke end of the piston and should not be interpreted. Solid lines denote averaged, normalized data. Dashed lines denote fitted velocities using equation (10). Arrow indicates the loading up to the target value of σ_{ax}.

in the surrounding and supposedly stiffer materials [*Rutter et al.*, 2009].

6. Conclusion

[56] We performed drained dehydration tests on Volterra gypsum in hydrostatic and creep conditions, while monitoring AEs and elastic wave velocities. The dehydration reaction of gypsum into bassanite and water induces a large porosity increase, which is partially compacted. The higher the effective stress, the larger the compaction. Application of a constant differential stress results in a faster axial compaction. The dehydration reaction is associated with a swarm of AE activity, which is mainly due to compaction as demonstrated by the focal mechanisms of the AEs. During the reaction, P and S wave velocities decrease, as well as Poisson's ratio. By using a differential effective medium model, the evolution of elastic moduli is explained by (1) the formation of low aspect ratio (0.05) spheroidal pores and (2) replacement of gypsum by bassanite. In situ observations

of the microstructure during dehydration were carried out in an ESEM. They reveal that the onset of dehydration is marked by the formation of thin intragranular cracks, and then by grain boundary opening.

[57] Our data and model strongly suggest that the signature of dehydrating rocks in seismic tomography should be low V_P and V_S, as well as a low V_P/V_S ratio. The possible enhancement of elastic anisotropy due to crystal preferred orientations by oriented microcracking is a major issue in the interpretation of what may be an apparent Poisson's ratio. Indeed, the effect of pore pressure on Poisson's ratio is not expected to be dominant over the effect of anisotropy.

[58] Localization of deformation and dynamic faulting was not observed during the dehydration test performed at constant differential stress, which is consistent with recent experiments on serpentinite [*Rutter et al.*, 2009; *Chernak and Hirth*, 2010; *Gasc et al.*, 2011]. However, the substantial compaction (up to 10%) observed during the dehydration reaction indicates the high deformability of dehydrating rocks. The exact rheology of dehydrating rocks, such as Volterra gypsum, yet remains to be determined by more systematic experiments performed at various fixed differential stresses. Nevertheless, we qualitatively argue that dehydration reactions can induce strain and/or stress concentrations in the surrounding rocks, which may eventually produce the so-called dehydration-induced earthquakes.

Appendix A: Calculation of the Extent of Reaction During Hydrostatic Tests

[59] From the stoechiometry of reaction (1), an increment in reaction progress $d\xi$ induces an increment dm_{tot} of the total fluid mass in the porous network:

$$dm_{tot} = \frac{3}{2}\frac{M_{water}}{M_{gypsum}}\rho_{gypsum}V_{sample}(1-n_0)d\xi, \quad \text{(A1)}$$

where n_0 is the starting porosity of the sample (other notations can be found in Table 2). Since the initial porosity is negligible compared to the created porosity, in the following we assume that $1 - n_0 \approx 1$.

[60] An independent expression of the total fluid mass within the porous network is

$$m_{tot} = \rho_f(T_0)V_Q + \rho_f(T)(V_{pore} + V_{tubing}), \quad \text{(A2)}$$

1where $\rho_f(T_0)$ is the density of water at room temperature (within the pore pressure pump), $\rho_f(T)$ is the density of water at the temperature of the sample, $V_{pore} = nV_{sample}$ is the pore volume, V_{tubing} is the tubing volume and V_Q is the pump volume. From expression A2, the fluid mass increment is written

$$
\begin{aligned}
dm_{tot} &= \rho_f(T_0)dV_Q + \rho_f(T)V_{sample}dn + nV_{sample}d\rho_f \\
&\quad + \rho_f(T)dV_{tubing} + V_{tubing}d\rho_f, \\
&= \rho_f(T_0)dV_Q + \rho_f(T)V_{sample}\left[dn_c + \frac{\partial n}{\partial \xi}d\xi\right] \\
&\quad + \left[V_{sample}\left(\rho_f(T)\frac{\partial n}{\partial T} + n\frac{\partial \rho_f}{\partial T}\right) + \rho_f(T)\frac{\partial V_{tubing}}{\partial T}\right] \\
&\quad + V_{tubing}\frac{\partial \rho_f}{\partial T}\Bigg]dT, \quad \text{(A3)}
\end{aligned}
$$

where n is the porosity of the sample, dn_c is the porosity change due to inelastic compaction and $(\partial n)/(\partial \xi)d\xi$ is the porosity change due to the solid volume change of the reaction. Neglecting the relative changes in fluid volume contained in the tubing system in comparison to the volume changes due to porosity compaction and creation, we obtain

$$dm_{tot} \approx \rho_f(T_0)dV_Q + \rho_f(T)V_{sample}\left[dn_c + \frac{\partial n}{\partial \xi}d\xi\right]. \quad (A4)$$

[61] The porosity change due to an increment in reaction extent is estimated from the molar volumes of the phases and the stoichiometry of the reaction:

$$\frac{\partial n}{\partial \xi} = 1 - \frac{V_{bass}}{V_{gypsum}}, \quad (A5)$$

where V_{bass} and V_{gypsum} are the molar volumes of bassanite and gypsum, respectively. The temperature dependency of these parameters is neglected.

[62] The combination of equations (A1), (A4), and (A5) yields the following expression for the increment of reaction extent:

$$d\xi = \left[\rho_f(T_0)\frac{dV_Q}{V_{sample}} + \rho_f(T)dn_c\right]$$
$$\Big/\left[\frac{3}{2}\frac{M_{water}}{M_{gypsum}}\rho_{gypsum} - \rho_f(T)\left(1 - \frac{V_{bass}}{V_{gypsum}}\right)\right]. \quad (A6)$$

Appendix B: Differential Effective Medium Model

[63] Pores are modeled as spheroids, which are characterized by their aspect ratio α. For $\alpha < 1$, pores are oblate or "crack-like"; for $\alpha > 1$, pore are prolate or "needle-like." The limiting cases of $\alpha \to 0$, $\alpha \to \infty$ and $\alpha = 1$ correspond to infinitely thin cracks, infinitely long needles, and spherical pores, respectively.

[64] Let us consider an isotropic solid matrix of bulk and shear moduli (K^0, G^0), respectively, containing randomly oriented spheroidal pores having the same aspect ratio α. According to the DEM scheme, the effective bulk and shear moduli (K, G), as functions of the porosity n, are described by a pair of coupled differential equations:

$$(1-n)\frac{1}{K}\frac{dK}{dn} = -(1-\zeta)P(\nu, \zeta; \alpha),$$
$$(1-n)\frac{1}{G}\frac{dG}{dn} = -Q(\nu, \zeta; \alpha), \quad (B1)$$

with the initial conditions $K(n=0) = K^0$ and $G(n=0) = G^0$. The undrained pore compressibility P and shear compliance Q are cumbersome functions of α, ν, the effective Poisson's ratio, and $\zeta = K_f/K$, where K_f is the bulk modulus of the saturating fluid. They are given by Berryman [1980].

[65] The differential system B1 is solved numerically by a fourth-order Runge-Kutta integration method (function ODE45 in Matlab). Formally, we have then access to a function that calculates the effective moduli as a function of porosity, solid matrix moduli, aspect ratio and fluid bulk modulus.

[66] The solid matrix moduli evolve during the dehydration reaction, as gypsum is progressively replaced by bassanite. In absence of any a priori information on the spatial organization of the two phases, they are estimated by a geometric mean [cf. Tarantola, 2006]:

$$K^0(\xi) = (K^0_{gypsum})^{(1-\xi)}(K^0_{bass})^\xi, \quad (B2)$$

$$G^0(\xi) = (G^0_{gypsum})^{(1-\xi)}(G^0_{bass})^\xi. \quad (B3)$$

The notations and values are reported in Table 2. The shear modulus of bassanite could not be found in published literature, and we assumed a value consistent with the velocity measurements by trial and error. During the reaction, the porosity and thus the density of the rock evolves. The evolution of porosity is estimated from the reaction progress, solid volume change and measured compaction as

$$n(\xi(t)) = \left(1 - \frac{V_{bass}}{V_{gypsum}}\right)\xi(t) + \Delta n_c(t). \quad (B4)$$

The density is then

$$\rho(\xi) = [(1-\xi)\rho_{gypsum} + \xi\rho_{bass}](1 - n(\xi)) + \rho_f n(\xi). \quad (B5)$$

[67] Recalling the expressions of P and S wave velocities as a function of elastic moduli and density,

$$V_P = \sqrt{\frac{K + (4/3)G}{\rho}}, \quad (B6)$$

$$V_S = \sqrt{\frac{G}{\rho}}, \quad (B7)$$

we conclude that the combination of equations (B1)–(B7) leads to a direct relation between P and S wave speeds and aspect ratio α. Formally we write

$$(V_P^{calc}, V_S^{calc}) = \mathbf{f}_\xi(\alpha) \quad (B8)$$

for any value of $\xi(t)$. The formal relation (B8) is used to invert the aspect ratio evolution during the two hydrostatic experiments (in which $\xi(t)$ could be estimated).

[68] The inversion procedure is probabilistic [Tarantola, 2005]. The wave speed data is assumed to follow a double exponential probability distribution with a mean error $\sigma_V = 50$ m s^{-1}. For each measurement (V_P^{obs}, V_S^{obs}), the posterior probability density

$$\rho(\alpha) = \exp\left(-\frac{|V_P^{obs} - V_P^{calc}| + |V_S^{obs} - V_S^{calc}|}{\sigma_V}\right) \quad (B9)$$

is calculated. The maximum of $\rho(\alpha)$ gives the "best" (in the sense of the least absolute values criterion) aspect ratio α that fits the observed velocity values.

References

Adelinet, M., J. Fortin, Y. Guéguen, A. Schubnel, and L. Geoffroy (2010), Frequency and fluid effects on elastic properties of basalt: Experimental investigations, *Geophys. Res. Lett.*, *37*, L02303, doi:10.1029/2009GL041660.

Ahrens, T. J. (Ed.) (1995), *Mineral Physics and Crystallography: A Handbook of Physical Constants*, AGU, Washington, D. C.

Arkwright, J. C., E. H. Rutter, K. H. Brodie, and S. Llana-Fúnez (2008), Role of porosity and dehydration reactions on the deformation of hot-pressed serpentinite aggregates, *J. Geol. Soc.*, *165*, 639–649.

Ayling, M. R., P. G. Meredith, and S. A. F. Murrell (1995), Microcracking during triaxial deformation of porous rocks monitored by changes in rock physical properties, I. Elastic-wave propagation measurements on dry rocks, *Tectonophysics*, *245*, 205–221.

Berman, R. G. (1991), Thermobarometry using multi-equilibrium calculations: A new technique, with petrological applications, *Can. Mineral.*, *29*(4), 833–855.

Berryman, J. G. (1980), Long-wavelength propagation in composite elastic media II. Ellipsoidal inclusions, *J. Acoust. Soc. Am.*, *68*(6), 1820–1831.

Brantut, N., A. Schubnel, and Y. Guéguen (2011), Damage and rupture dynamics at the brittle-ductile transition: The case of gypsum, *J. Geophys. Res.*, *116*, B01404, doi:10.1029/2010JB007675.

Budiansky, B., and R. J. O'Connell (1976), Elastic moduli of a cracked solid, *Int. J. Solids Struct.*, *12*, 81–97.

Burlini, L., G. Di Toro, and P. Meredith (2009), Seismic tremor in subduction zones: Rock physics evidence, *Geophys. Res. Lett.*, *36*, L08305, doi:10.1029/2009GL037735.

Chernak, L. J., and G. Hirth (2010), Deformation of antigorite serpentinite at high temperature and pressure, *Earth Planet. Sci. Lett.*, *29*, 23–33.

Chernak, L. J., and G. Hirth (2011), Syndeformational antigorite dehydration produces stable fault slip, *Geology*, *39*(9), 847–850, doi:10.1130/G31919.1.

Christensen, N. I. (1984), Pore pressure and oceanic crustal seismic structure, *Geophys. J. R. Astron. Soc.*, *79*, 411–423.

Comodi, P., S. Nazzareni, L. Dubrovinsky, and M. Merlini (2009), The high-pressure–high-temperature behavior of bassanite, *Am. Mineral.*, *94*, 1596–1602.

Connolly, J. A. D. (1997), Devolatilization-generated fluid pressure and deformation-propagated fluid flow during prograde regional metamorphism, *J. Geophys. Res.*, *102*(B8), 18,149–18,173.

David, E. C., and R. W. Zimmerman (2011a), Compressibility and shear compliance of spheroidal pores: Exact derivation via the Eshelby tensor, and asymptotic expressions in limiting cases, *Int. J. Solids Struct.*, *48*, 680–686.

David, E. C., and R. W. Zimmerman (2011b), Elastic moduli of solids containing spheroidal pores, *Int. J. Eng. Sci.*, *49*(7), 544–560.

Deer, W. A., R. A. Howie, and J. Zussman (1966), *An Introduction to the Rock-Forming Minerals*, John Wiley, New York.

Dobson, D. P., P. G. Meredith, and S. A. Boon (2002), Simulation of subduction zone seismicity by dehydration of serpentine, *Science*, *258*, 1407–1410.

Feigner, B., and R. P. Young (1992), Moment tensor inversion of induced microseismic events: Evidence of non-shear failures in the $-4 < M < -2$ moment magnitude range, *Geophys. Res. Lett.*, *19*, 1503–1506.

Fortin, J., Y. Guéguen, and A. Schubnel (2007), Effects of pore collapse and grain crushing on ultrasonic velocities and v_p/v_s, *J. Geophys. Res.*, *112*, B08207, doi:10.1029/2005JB004005.

Fortin, J., S. Stanchits, G. Dresen, and Y. Guéguen (2009), Acoustic emissions monitoring during inelastic deformation of porous sandstone: Comparison of three modes of deformation, *Pure Appl. Geophys.*, *66*, 823–841, doi:10.1007/s00024-009-0479-0.

Fusseis, F., C. Schrank, J. Liu, A. Karrech, S. Llana-Fùnez, X. Xiao, and K. Regenauer-Lieb (2011), Pore formation during dehydration of polycristalline gypsum observed and quantified in a time-series synchrotron radiation based x-ray micro-tomography experiment, *Solid Earth Discuss.*, *3*, 857–900.

Gasc, J., A. Schubnel, F. Brunet, S. Guillon, H.-J. Mueller, and C. Lathe (2011), Simultaneous acoustic emissions monitoring and synchrotron x-ray diffraction at high pressure and temperature: Calibration and application to serpentinite dehydration, *Phys. Earth Planet. Inter.*, *189*(3–4), 121–133.

Green, H. W., and H. Houston (1995), The mechanics of deep earthquakes, *Annu. Rev. Earth Planet. Sci.*, *23*, 169–213.

Guéguen, Y., and J. Dienes (1989), Transport properties of rocks from statistics and percolation, *Math. Geol.*, *21*(1), 1–13.

Guéguen, Y., and V. Palciauskas (1994), *Introduction to the Physics of Rocks*, Princeton Univ. Press, Princeton, N. J.

Gupta, I. N. (1973), Seismic velocities in rock subjected to axial loading up to shear fracture, *J. Geophys. Res.*, *78*(29), 6936–6942.

Hacker, B. R., S. M. Peacock, G. A. Abers, and S. D. Holloway (2003), Subduction factory: 2. Are intermediate-depth earthquakes in subducting slabs linked to metamorphic dehydration reactions?, *J. Geophys. Res.*, *108*(B1), 2030, doi:10.1029/2001JB001129.

Heard, H. C., and W. W. Rubey (1966), Tectonic implications of gypsum dehydration, *Geol. Soc. Am. Bull.*, *77*, 741–760.

Henyey, F. S., and N. Pomphrey (1982), Self-consistent elastic moduli of a cracked solid, *Geophys. Res. Lett.*, *9*(8), 903–906.

Hirose, T., M. Bystricky, K. Kunze, and H. Stünitz (2006), Semi-brittle flow during dehydration of lizardite-chrysotile serpentinite deformed in torsion: Implication for the rheology of oceanic lithosphere, *Earth Planet. Sci. Lett.*, *249*, 484–493.

Hudson, J., R. Pearce, and R. Rogers (1989), Source type plot for inversion of the moment tensor, *J. Geophys. Res.*, *94*(B1), 765–774.

Jung, H., H. W. Green, and L. F. Dobrzhinetskaya (2004), Intermediate depth earthquake faulting by dehydration embrittlement with negative volume change, *Nature*, *428*, 545–549.

Jung, H., Y. Fei, P. G. Silver, and H. W. Green (2009), Frictional sliding in serpentine at very high pressure, *Earth Planet. Sci. Lett.*, *277*, 273–279.

Katayama, I., K. Hirauchi, K. Michibayashi, and J. Ando (2009), Trench-parallel anisotropy produced by serpentine deformation in the hydrated mantle wedge, *Nature*, *461*, 1114–1117, doi:10.1038/nature08513.

Kirby, S. H. (1987), Localized polymorphic phase transformations in high-pressure faults and applications to the physical mechanism of deep earthquakes, *J. Geophys. Res.*, *92*(B13), 13,789–13,800.

Ko, S.-C., D. L. Olgaard, and U. Briegel (1995), The transition from weakening to strengthening in dehydrating gypsum: Evolution of excess pore pressures, *Geophys. Res. Lett.*, *22*(9), 1009–1012.

Ko, S.-C., D. L. Olgaard, and T.-F. Wong (1997), Generation and maintenance of pore pressure excess in a dehydrating system: 1. Experimental and microstructural observations, *J. Geophys. Res.*, *102*(B1), 825–839.

Kuster, G. T., and M. N. Toksoz (1974), Velocity and attenuation of seismic waves in two-phase media: Part I. Theoretical formulations, *Geophysics*, *39*, 587–606.

Le Ravalec, M., and Y. Guéguen (1996), High- and low-frequency elastic moduli for a saturated porous/cracked rock; differential self-consistent and poroelastic theories, *Geophysics*, *61*, 1080–1094.

Llana-Fúnez, S., K. H. Brodie, E. H. Rutter, and J. C. Arkwright (2007), Experimental dehydration kinetics of serpentinite using pore volumometry, *J. Metamorph. Geol.*, *25*, 423–438.

Lockner, D., and J. Byerlee (1977), Acoustic emission and creep in rock at high confining pressure and differential stress, *Bull. Seismol. Soc. Am.*, *67*(2), 247–258.

Mavko, G., and A. Nur (1975), Melt squirt in the asthenosphere, *J. Geophys. Res.*, *80*(11), 1444–1448.

McConnell, J. D. C., D. M. Astill, and P. L. Hall (1987), The pressure dependence of the dehydration of gypsum to bassanite, *Mineral. Mag.*, *51*, 453–457.

McLaughlin, R. (1977), A study of the differential scheme for composite materials, *Int. J. Eng. Sci.*, *15*, 237–244.

Milsch, H., and C. H. Scholz (2005), Dehydration-induced weakening and fault slip in gypsum: Implications for the faulting process at intermediate depth in subduction zones, *J. Geophys. Res.*, *110*, B04202, doi:10.1029/2004JB003324.

Milsch, H., W. Heinrich, and G. Dresen (2003), Reaction-induced fluid flow in synthetic quartz-bearing marbles, *Contrib. Mineral. Petrol.*, *146*, 286–296.

Murrell, S. A. F., and I. A. H. Ismail (1976), The effect of decomposition of hydrous minerals on the mechanical properties of rocks, *Tectonophysics*, *31*, 207–258.

Norris, A. N. (1985), A differential scheme for the effective moduli of composites, *Mech. Mater.*, *4*, 1–16.

O'Connell, R. J., and B. Budiansky (1974), Seismic velocities in dry and saturated cracked solids, *J. Geophys. Res.*, *79*(35), 5412–5426.

Olgaard, D. L., S.-C. Ko, and T.-F. Wong (1995), Deformation and pore pressure in dehydrating gypsum under transiently drained conditions, *Tectonophysics*, *245*, 237–248.

Ougier-Simonin, A., J. Fortin, Y. Guéguen, A. Schubnel, and F. Bouyer (2011), Cracks in glass under triaxial conditions, *Int. J. Eng. Sci.*, *49*(1), 105–121.

Peacock, S. M., N. I. Christensen, M. G. Bostock, and P. Audet (2011), High pore pressures and porosity at 35 km depth in the Cascadia subduction zone, *Geology*, *39*(5), 471–474, doi:10.1130/G31649.1.

Popp, T., and H. Kern (1993), Thermal dehydration reactions characterised by combined measurements of electrical conductivity and elastic wave velocities, *Earth Planet. Sci. Lett.*, *120*, 43–47.

Raleigh, C. B., and M. S. Paterson (1965), Experimental deformation of serpentinite and its tectonic implications, *J. Geophys. Res.*, *70*(16), 3965–3985.

Reynard, B., J. Nakajima, and H. Kawakatsu (2010), Earthquakes and plastic deformation of anhydrous slab mantle in double Wadati-Benioff zones, *Geophys. Res. Lett.*, *37*, L24309, doi:10.1029/2010GL045494.

Robie, R. A., B. S. Hemingway, and J. R. Fisher (1979), Thermodynamic properties of minerals and related substances at 298.15 K and 1 bar (10^5 pascals) pressure and at higher temperatures, *U.S. Geol. Surv. Bull.*, *1452*.

Rutter, E. H., and K. H. Brodie (1988), Experimental "syntectonic" dehydration of serpentinite under conditions of controlled pore water pressure, *J. Geophys. Res.*, *93*(B5), 4907–4932.

Rutter, E. H., and K. H. Brodie (1995), Mechanistic interactions between deformation and metamorphism, *Geol. J.*, *30*, 227–240.

Rutter, E. H., S. Llana-Fùnez, and K. H. Brodie (2009), Dehydration and deformation of intact cylinders of serpentinite, *J. Struct. Geol.*, *31*, 29–43, doi:10.1016/j.jsg.2008.09.008.

Salganik, R. L. (1973), Mechanics of bodies with many cracks, *Mech. Solids*, *8*(4), 135–143.

Sayers, C., and M. Kachanov (1995), Microcrack-induced elastic wave anisotropy of brittle rocks, *J. Geophys. Res.*, *100*(B3), 4149–4156.

Schubnel, A., O. Nishizawa, K. Masuda, X. J. Lei, Z. Xue, and Y. Guéguen (2003), Velocity measurements and crack density determination during wet triaxial experiments on Oshima and Toki granites, *Pure Appl. Geophys.*, *160*, 869–887.

Sipple, E.-M., P. Braconi, P. Dufour, and J.-C. Mutin (2001), Microstructural modifications resulting from the dehydration of gypsum, *Solid State Ionics*, *141–142*, 447–454.

Stretton, I. C. (1996), An experimental investigation of the deformation properties of gypsum, PhD thesis, Univ. of Manchester, Manchester, U. K.

Stretton, I. C., P. F. Schofield, S. Hull, and K. S. Knight (1997), The static compressibility of gypsum, *Geophys. Res. Lett.*, *24*(10), 1267–1270.

Tarantola, A. (2005), *Inverse Problem Theory*, 2nd ed., Soc. for Ind. and Appl. Math., Philadelphia, Pa.

Tarantola, A. (2006), *Elements for Physics*, Springer, Berlin.

Thomsen, L. (1986), Weak elastic anisotropy, *Geophysics*, *51*(10), 1954–1966.

Walsh, J. B. (1965), The effect of cracks on the compressibility of rock, *J. Geophys. Res.*, *70*(2), 381–389.

Wang, W. H., and T.-F. Wong (2003), Effects of reaction kinetics and fluid drainage on the development of pore pressure excess in a dehydrating system, *Tectonophysics*, *370*, 227–239, doi:10.1016/S0040-1951(03)00188-4.

Wang, Z., and A. Nur (1990), Dispersion analysis of acoustic velocities in rocks, *J. Acoust. Soc. Am.*, *87*(6), 2384–2395.

Wong, T.-F., S.-C. Ko, and D. L. Olgaard (1997), Generation and maintenance of pore pressure excess in a dehydrating system: 2. Theoretical analysis, *J. Geophys. Res.*, *102*(B1), 841–852.

Yamasaki, T., and T. Seno (2003), Double seismic zone and dehydration embrittlement of the subducting slab, *J. Geophys. Res.*, *108*(B4), 2212, doi:10.1029/2002JB001918.

Zimmerman, R. W. (1991a), *Compressibility of Sandstones*, Elsevier, Amsterdam.

Zimmerman, R. W. (1991b), Elastic moduli of a solid containing spherical inclusions, *Mech. Mater.*, *12*, 17–24.

N. Brantut, Rock and Ice Physics Laboratory, Department of Earth Science, University College London, Gower Street, London WC1E 6BT, UK. (nicolas.brantut@normalesup.org)

E. C. David, Department of Earth Science and Engineering, Imperial College London, London SW7 2AZ, UK.

A. Dimanov and E. Héripré, Laboratoire de Mécanique des Solides, CNRS UMR 7649, École Polytechnique, F-91128 Palaiseau CEDEX, France.

Y. Guéguen and A. Schubnel, Laboratoire de Géologie, École Normale Supérieure, 24 rue Lhomond, F-75231 Paris CEDEX 5, France.